Research Article Vol. 33, No. 26 / 29 Dec 2025 / Optics Express 54879
Optics EXPRESS

Single-ended forward-transmission distributed sensing system based on chirped frequency-swept modulation

SHANGWEI DAI,[1,2] HANJIE LIU,[1,2] XING RAO,[1,2] DANXIA LU,[1,2] LINQIAO DU,[1,2] YIPING WANG,[1,2] AND GEORGE Y. CHEN[1,2,*]

[1]State Key Laboratory of Radio Frequency Heterogeneous Integration, Key Laboratory of Optoelectronic Devices and Systems of Ministry of Education/Guangdong Province, College of Physics and Optoelectronic Engineering, Shenzhen University, Shenzhen 518060, China
[2]Shenzhen Key Laboratory of Ultrafast Laser Micro/Nano Manufacturing, Guangdong and Hong Kong Joint Research Centre for Optical Fibre Sensors, Shenzhen University, Shenzhen 518060, China
*gychen@szu.edu.cn

Abstract: In a rapidly urbanizing world with a heavy investment in mega infrastructures, ultra-long-distance sensing enables critical structural health monitoring and natural disaster early warning. Forward-transmission distributed fiber-optic sensing offers unique advantages including hundred-kilometer-scale sensing distances and mega-hertz detection bandwidth. To meet the practical application requirements of single-ended probing and electrically passive fiber termination, we propose a single-ended, forward-transmission distributed fiber-optic vibration sensing (FTDVS) system based on single-sideband chirped frequency-swept modulation using an I/Q modulator. At the termination end, two segments of delay fibers facilitate frequency-domain separation to distinguish specific forward-propagating optical paths from unwanted paths, while digital filters eliminate Rayleigh backscattering (RBS) and extract the sensing signals. This system employs standard telecom single-mode fiber for sensing and avoids the need for wavelength-division multiplexers (WDM) and multi-wavelength laser sources, thus reducing complexity and cost. The experimental results demonstrate robust performance under extreme conditions involving RBS being 72 dB stronger than forward-propagating light, achieving 85 m in positioning accuracy over a single-span sensing distance of 120 km without inline amplification. This work paves the way for long-distance distributed mapping and ground-truthing of infrastructure and the environment, which forms the backbone of smart cities.

1. Introduction

Distributed optical fiber sensing (DOFS) is a powerful technology that transforms an optical fiber into the equivalent of a continuous array of thousands or tens of thousands of sensors. A forward transmission distributed vibration sensing (FTDVS) system utilizes the transmitted light of a continuous-wave light source, rather than relying on weak Rayleigh backscattering (RBS) for probing the optical fiber for perturbations [1]. This class of methods offer a unique combination of advantages compared with conventional reflectometry methods, such as ultra-long sensing distances, high sensitivity, wide frequency response range [2], and ease of integration with existing communication systems [3–6]. These sensing systems can be widely applied in areas such as earthquake early warning [7–9], traffic-pavement monitoring [10], and high-speed railway track structural health assessment [11]. Unlike traditional distributed acoustic sensing (DAS) systems that utilize phase-sensitive optical time-domain reflectometry (Φ-OTDR), which rely on the time-of-flight (ToF) method for event positioning [12], FTDVS determine positions based on the difference in time-of-arrival between polarization or phase signals of the two detection ends [13,14]. However, double-ended systems introduce significant practical engineering challenges,

#579573 https://doi.org/10.1364/OE.579573
Journal © 2025 Received 24 Sep 2025; revised 11 Dec 2025; accepted 15 Dec 2025; published 23 Dec 2025

Optics EXPRESS

and are not suitable for boreholes or access-limited environments. More importantly, synchronized data processing [15] at the two detection ends is cumbersome and impractical, thus most designs co-locate the hardware into a single unit and utilize a fiber loop configuration. As a result, single-ended systems offer superior deployment versatility and broadens the application scope.

A single-ended system is defined as a system with co-located laser and demodulation subsystems, avoiding large-scale loop deployment of the sensing fiber. This configuration prevents crosstalk scenarios where a single perturbation simultaneously affects multiple positions along the fiber, which is a limitation typically seen in loop-based architectures. The fundamental setup resembles an in-line Sagnac interferometer (SI). For example, X. Fang purposed a two-loop Sagnac interferometer, it involves placing a Faraday rotator mirror (FRM) at the far end of the sensing fiber to reflect the probe light back while maintaining a consistent polarization state before and after reflection [16]. Alternatively, J. Ali, et al used two parallel sensing fibers as the sensor element, connected at their far ends [17]. In this case, the sensing light returning to the receiver experiences the same perturbation twice. The position of the vibration can be deduced by extracting the null-frequency points [18] or by using the cepstrum analysis to determine the phase delay difference between two identical perturbations [19]. However, both calculation methods are severely limited by the required perturbation bandwidth. Huang, et al. used a wavelength division multiplexer (WDM) to separate light traversing different paths for independent phase demodulation [20]. The phase delay difference can then be obtained using simple cross-correlation, which overcomes the bandwidth limitations of the notch point and cepstrum methods, offering more accurate delay estimation. However, phase change induced by perturbations varies depending on wavelength, leading to weaker correlation between the phase signals and reduced positioning accuracy [21]. W. Kong, et al have proposed using an ultra-narrow linewidth laser as the light source. At the termination end, an acousto-optic modulator (AOM) shifts the optical frequency of one path. This results in the different beat frequencies of the interference signals at the demodulation end. Performing phase reconstruction and cross-correlation on each signal yield the phase delay [22]. However, this method requires providing an electrical drive signal to the AOM at the termination end, which is high risk for combustive or remote environments. Additionally, this approach necessitates dual-core fiber for bidirectional transmission, further increasing deployment costs.

To realize passive termination of a single-ended sensing system while suppressing RBS crosstalk, this work proposes a chirped frequency-swept forward-transmission distributed sensing system (CFS-FTDVS). The system employs an I/Q modulator (IQM) to implement suppressed-carrier single-sideband modulation (SC-SSB) of a narrow-linewidth, linearly polarized laser, generating linearly swept-frequency probe light. At the terminal fiber end, an optical circulator serves as the input/output interface, preventing remote RBS contribution. Two distinct-length delay fibers separate forward-propagating light from other optical paths in the frequency domain, while a digital filter extracts the probe signal. Using standard telecom single-mode fiber (SMF) as the sensing medium, the all-passive termination design significantly extends applicability, particularly for ultra-long-distance distributed sensing in remote or inaccessible areas. This work lays the groundwork for unprecedented long-distance distributed mapping and ground-truthing of infrastructure and the environment, which is essential for developing smart cities and effective early-warning systems.

2. Theory

2.1. System design

The system configuration and schematic of the CFS-FTDVS are shown in Fig. 1(a). A narrow-linewidth (100 Hz linewidth), single-frequency, linearly polarized laser (Thorlabs, ULN15TK) emits continuous-wave light at 1550 nm into an IQM, which is driven by two chirped frequency-swept (CFS) signals: $RF_I = K\sin(2\pi f_m t + \pi\gamma t^2)$, $RF_Q = K\cos(2\pi f_m t + \pi\gamma t^2)$ generated by an

Optics EXPRESS

arbitrary waveform generator (AWG). Where f_m is the initial frequency and γ is the sweep rate. The signals are swept from 250 MHz to 750 MHz with a sweep period of 10 ms and a repetition frequency of 100 Hz, thus achieving a sweep rate γ of 50 GHz/s. The IQM is composed of two Mach-Zehnder modulator (MZM) and a 90° phase shifter, as shown in Fig. 1(b). When the RF signal is fed to the two MZMs, an automatic bias controller generates and maintains a bias voltage at the quadrature point through PID control and applies them to each modulator. These quadrature-point bias voltages ensure that both MZM inside the I/Q modulator operate in push-pull mode (i.e., modulation signals in the two arms of each MZM maintain a 180° phase difference). Therefore, the single-frequency continuous-wave light input to the IQM is phase-modulated by$K\sin(2\pi f_m t + \pi\gamma t^2)$, $-K\sin(2\pi f_m t + \pi\gamma t^2)$, $K\cos(2\pi f_m t + \pi\gamma t^2)$ and $-K\cos(2\pi f_m t + \pi\gamma t^2)$, respectively. Where is K modulation depth. To summarize, the optical field E_{out} output from the I/Q modulator can be expressed as:

$$\begin{aligned} E_{\text{out}}(t) = \exp(i2\pi f_0 t)\{&\exp(iK\cos\Omega(t)) + \exp(-iK\cos\Omega(t))\exp(i\pi) \\ &+[\exp(iK\sin\Omega(t)) + \exp(-iK\sin\Omega(t)) \times \exp(i\pi)]\exp(i\pi/2)\} \end{aligned} \tag{1}$$

where $\Omega(t) = 2\pi f_m t + \pi\gamma t^2$. Performing a first-order Bayesian expansion on the expression above and regrouping the terms yield:

$$\begin{aligned} E_{\text{out}}(t) = &J_{+1}(K)\exp(\pi\gamma t^2 + 2\pi f_0 t + 2\pi f_m t) \\ &+ J_{-3}(K)\exp(-3\pi\gamma t^2 + 2\pi f_0 t - 6\pi f_m t). \end{aligned} \tag{2}$$

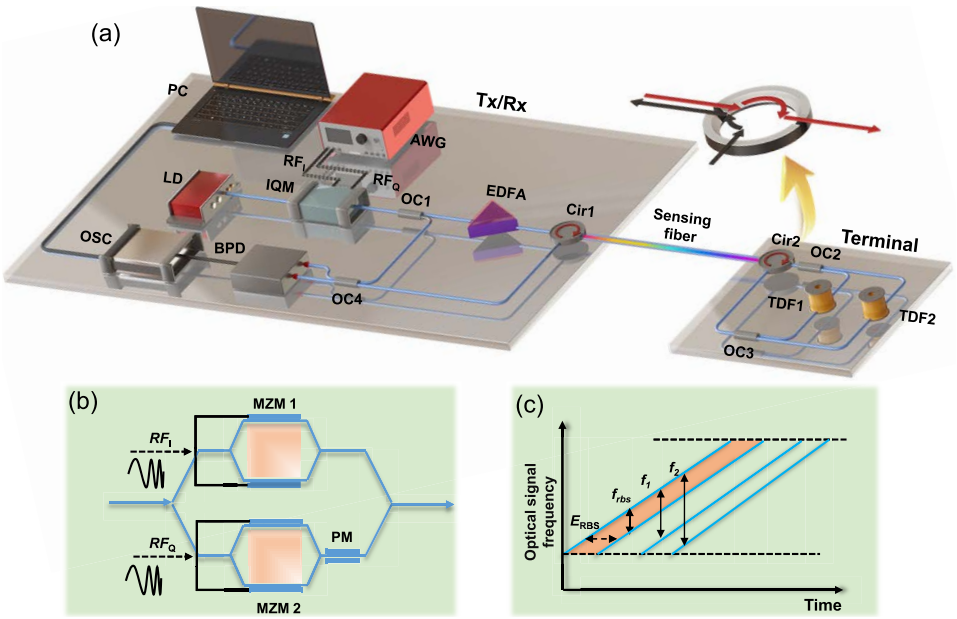

Fig. 1. CFS-FTDVS working principles: (a) System setup. Tx/Rx: transmitter/receiver, LD: laser diode, OC: optical coupler, IQM: in-phase/quadrature modulator, AWG: arbitrary waveform generator, EDFA: erbium-doped fiber amplifier, Cir: optical circulator, TDF: time-delay fiber, BPD: balanced photodetector, OSC: oscilloscope, PC: Personal computer, RF: radio frequency signal; (b) Structure of the I/Q modulator. MZM: Mach-Zehnder modulator, PM: phase modulator; (c) Optical frequency variation between I_{RBS}, I_1 and I_2.

Consequently, the +1-order sideband and -3-order sideband are retained while the carrier and other sidebands are suppressed. When the $K = 1.8$, the -3-order sideband experiences significant

Optics EXPRESS

suppression [23]. Thus, the optical frequency of the input light undergoes a SC-SSB sweep due to the CFS-RF modulation signal. The resulting CFS light exhibits sweep linearity essentially identical to that of the RF signal, thereby achieving excellent sweep linearity.

The CFS light is split into sensing light E_s and reference light E_r via OC1. The sensing light is then directed through Cir1 before being injected into the sensing fiber. After entering the sensing fiber, the optical signal is divided into two distinct propagation paths:

Path 1: Cir1→Sensing fiber→Cir2→TDF1→Cir2→Sensing fiber→Cir1→OC4.

Path 2: Cir1→Sensing fiber→Cir2→TDF2→Cir2→Sensing fiber→Cir1→OC4.

Due to the inherent unidirectional isolation of the optical circulator, RBS from the termination end cannot pass through the circulator back into the sensing fiber. The RBS propagation paths with weaker amplitudes are disregarded (see the Appendix for the full multi-path analysis); the dominant RBS path impacting the forward light is:

Path_{RBS}: Cir1→Sensing fiber→Cir1→OC4.

Consequently, the sensing light returned to the Rx through the Cir1 comprises the sum of optical fields from three distinct propagation paths: E_1, E_2 and E_{RBS}.

2.2. Rayleigh backscatter filtering

The optical field of the +1-order single-sideband probe light E_{out} output from Cir1 can be expressed as:

$$E_{out}(t) = E_r(t) = E_0 \exp[i(\pi\gamma t^2 + 2\pi f_0 t + 2\pi f_m t)] \tag{3}$$

where E_0 is the initial amplitude of optical field. After propagating through the three distinct paths, the optical fields returning to the Rx can be expressed respectively as:

$$E_s(t) = E_{RBS}(t) + E_1(t) + E_2(t) \tag{4}$$

$$E_{RBS}(t) = E_0 \sum_{\tau_l=0}^{\tau_L} R_{rbs}(\tau_l) \exp(i[\pi\gamma(t-\tau_l)^2 + 2\pi(f_0+f_m)(t-\tau_l) + \phi_{RBS}]) \tag{5}$$

$$E_1(t) = E_0 R_1 \exp(i[\pi\gamma(t-\tau_L-\tau_1)^2 + 2\pi(f_0+f_m)(t-\tau_L-\tau_1) + \phi_1]) \tag{6}$$

$$E_2(t) = E_0 R_2 \exp(i[\pi\gamma(t-\tau_L-\tau_2)^2 + 2\pi(f_0+f_m)(t-\tau_L-\tau_2) + \phi_2]) \tag{7}$$

where ϕ_1, ϕ_2 and ϕ_{RBS} are the phase shifts caused by an external disturbance which comprises a phase shift followed by the delayed second-pass phase shift, respectively. $\tau_L = 2nL/c$, $\tau_1 = nL_1/c$ and $\tau_2 = nL_2/c$ are the transit times in sensing fiber, TDF1 and TDF2, respectively. L, L_1 and L_2 are the lengths of sensing fiber, TDF1 and TDF2, respectively. c is the speed of light in vacuum, n is the effective index of the fiber, τ_l is the time-delay unit of the sensing light in the fiber. $R_{rbs}(\tau_l)$ is the propagation coefficient of RBS at τ_l. R_1 and R_2 are propagation coefficient of E_1 and E_2. They can be expressed as:

$$R_{rbs}(\tau_l) = \sqrt{\alpha_s \exp\left(-2\alpha\frac{c\tau_l}{n}\right)} \tag{8}$$

$$R_1 = \sqrt{\exp[-\alpha(2L+L_1)]} \tag{9}$$

$$R_2 = \sqrt{\exp[-\alpha(2L+L_2)]} \tag{10}$$

where α_s is the Rayleigh backscattering coefficient, α is the attenuation coefficient in SMF. The three aforementioned optical fields interfere with the E_r at the OC4, the resulting interference

Optics EXPRESS

intensity I_s can be expressed as:

$$I_s = I_{RBS} + I_1 + I_2 \tag{11}$$

$$\begin{aligned} I_{RBS}(t) &= |E_{RBS}(t) + E_r(t)|^2 \\ &= {E_0}^2 \sum_{\tau_l=0}^{\tau_L} \{1 + {R^2}_{rbs}(\tau_l) + 2R_{rbs}(\tau_l)\cos[2\pi(f_0 + f_m)\tau_l + 2\pi f_{rbs}t - \gamma{\tau_l}^2 + \phi_{RBS}]\} \end{aligned} \tag{12}$$

$$\begin{aligned} I_1(t) &= |E_1(t) + E_r(t)|^2 \\ &= {E^2}_0\{1 + {R^2}_1 + 2R_1\cos[2\pi(f_0 + f_m)(\tau_1 + \tau_L) + 2\pi f_1 t - \gamma(\tau_1 + \tau_L)^2 + \phi_1]\} \end{aligned} \tag{13}$$

$$\begin{aligned} I_2(t) &= |E_2(t) + E_r(t)|^2 \\ &= {E^2}_0\{1 + {R^2}_2 + 2R_2\cos[2\pi(f_0 + f_m)(\tau_2 + \tau_L) + 2\pi f_2 t - \gamma(\tau_2 + \tau_L)^2 + \phi_2]\} \end{aligned} \tag{14}$$

where I_{RBS}, I_1 and I_2 are the interference intensities generated by the E_1, E_2 and E_{RBS} interfering with E_r, respectively. Here we designate $I_{FW} = I_1 + I_2$ as the forward light intensity, and I_{RBS} as the RBS noise that requires filtering out. $f_{rbs} = \gamma\tau_l$ is the beat frequency of RBS interfering with E_r.$f_1 = (\tau_L + \tau_1) \times \gamma$, while $f_2 = (\tau_L + \tau_2) \times \gamma$ is the beat frequency from E_1, E_2 interfering with E_r. Figure 1(c) shows the optical frequency variation between I_{RBS}, I_1 and I_2. It can be seen from Eq. (12–14) that these three signals are spectrally separated, thereby enabling their individual isolation and extraction from the frequency spectrum. Figure 2(a) presents the frequency-domain, time-frequency domain and the time-domain representations of I_s when a sinusoidal perturbation is applied at a point along the 20 km sensing fiber. I_s then received by a BPD (200 MHz bandwidth), converted into an electrical signal, and fed into an oscilloscope with a sampling rate of 250 MHz. TDF1 and TDF2 must be sufficiently long to ensure that the central frequencies of I_1 and I_2 do not overlap in the frequency domain when vibration occurs on the sensing fiber. In the experiment, the lengths of TDF1 and TDF2 were are 9.760 km and 20.122 km, respectively. At this point, according to $\Delta f = (\tau_2 - \tau_1) \times n \times \gamma/c$, the separation between f_1 and f_2 is 2.53 MHz. This spacing accommodates most vibration-induced frequency broadening. Due to the superposition of multiple spectral components, I_s appears random/noisy in the time domain. Calculating its power spectral density (PSD) reveals that its spectral components can be broadly divided into three parts: I_{RBS}, I_1, and I_2. In the time-frequency representation, these three components are also visibly separate from each other, and sinusoidal oscillations are observable at frequencies f_1 and f_2. I_s is then filtered through two bandpass filters, corresponding to the different TDFs, yielding signals I_1 and I_2. Analysis of their frequency-domain and time-frequency domain results shown in Fig. 2(b) and (c) demonstrates that both approaches lead to a high signal-to-noise ratio (SNR).

2.3. Demodulation and positioning methods

The flowchart of the phase demodulation and positioning methods is shown in Fig. 3. When individually extracted signals I_1 and I_2 are obtained, the Hilbert transform can be utilized to construct analytic functions and thereby obtain their quadrature components. Taking I_1 as an example:

$$Hil[I_1(t)] = \sin\left(2\pi(f_0 + f_m)(\tau_1 + \tau_L) + f_1 t + \frac{1}{2}\gamma(\tau_1 + \tau_L)^2 + \phi_1\right) \tag{15}$$

By then performing I/Q demodulation [24] and filtering out the DC component, the vibration-induced phase signal can be obtained:

$$\phi_1(t) = \arctan\left(\frac{I_1(t)}{Hil[I_1(t)]}\right) - 2\pi f_1 t \tag{16}$$

When propagating through the sensing fiber, both E_1 and E_2 undergo phase changes induced by the same perturbation source twice. The phase changes in the optical fields induced by external

Optics EXPRESS

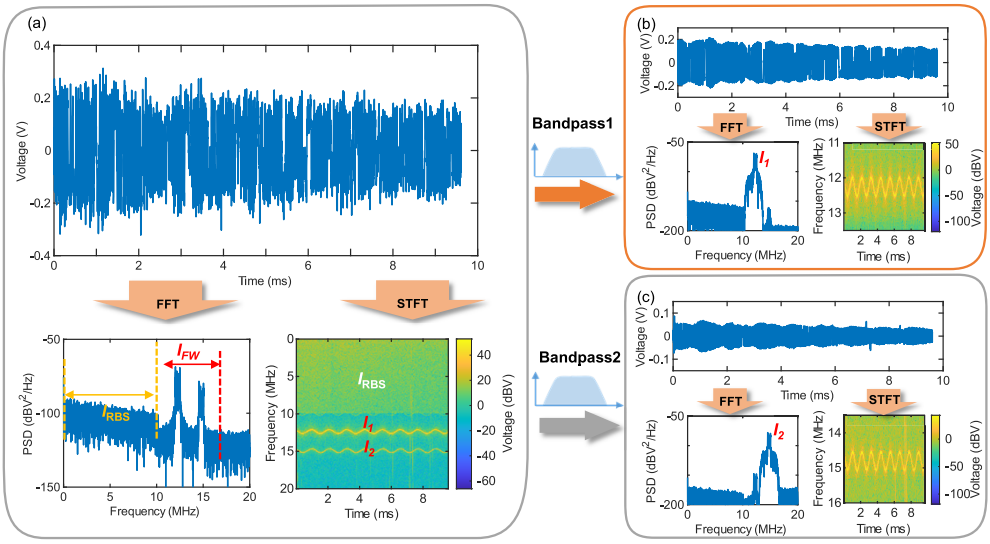

Fig. 2. Analysis of example vibration signal: (a) Time-domain, frequency-domain and time-frequency domain representations of I_s received by the BPD when a sinusoidal perturbation is applied at 20 km along the sensing fiber; (b) Multi-domain representations of I_1 after passing through Bandpass1; (c) Multi-domain representations of I_2 after passing through Bandpass2. FFT: Fast Fourier transform. STFT: short-time Fast Fourier transform.

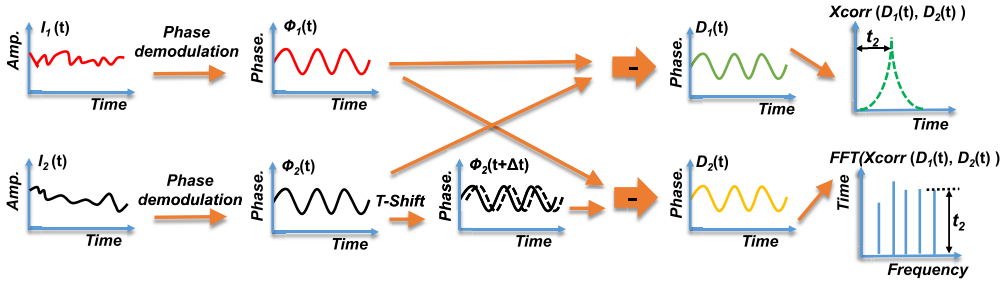

Fig. 3. Flowchart of the phase demodulation and positioning methods. T-shift: Time shift, Xcorr: cross-correlation.

perturbations along the two paths can be expressed as:

$$\phi_1(t) = \varphi(t) + \varphi(t - t_1) \tag{17}$$

$$\phi_2(t) = \varphi(t) + \varphi(t - t_2) \tag{18}$$

where t_1 and t_2 are the transit times in path: PZT->Cir2->TDF1->Cir2->PZT and PZT->Cir2->TDF2->Cir2->PZT, respectively. $\varphi(t)$ is the phase change induced by PZT. Two differential signals, D_1(t) and D_2(t), are constructed by:

$$D_1(t) = \phi_1(t) - \phi_2(t) \tag{19}$$

$$D_2(t) = \phi_2(t + \Delta t) - \phi_1(t) \tag{20}$$

$$\Delta t = t_2 - t_1 \tag{21}$$

Expand Eq. (19) and substitute in Eq. (20) to obtain:

$$D_1(t) = \phi_1(t) - \phi_2(t) = \varphi(t - t_1) - \varphi(t - t_2) \tag{22}$$

Optics EXPRESS

$$\begin{aligned} D_2(t-t_2) &= \phi_2(t-t_1) - \phi_1(t-t_2) \\ &= \varphi(t-t_1) + \varphi(t-t_1-t_2) - \varphi(t-t_2) - \varphi(t-t_1-t_2) \\ &= \varphi(t-t_1) - \varphi(t-t_2) \end{aligned} \tag{23}$$

It is evident that $D_1(t) = D_2(t-t_2)$. Performing cross-correlation between $D_1(t)$ and $D_2(t)$ yields the time delay t_2. The vibration position along the sensing fiber can be calculated by:

$$Z = \frac{(2\tau_L - t_2 + \tau_2)c}{2n} \tag{24}$$

3. Experiment results

3.1. Spectral noise analysis

In the single-core, single-mode, bidirectional propagation scheme, the Rx inevitably receives RBS noise. To investigate the impact of RBS on the forward-propagating signal, the performance of using sensing fibers of varying lengths were compared, through acquiring interference intensity signals and computed their PSD. From 70 km onwards, an erbium-doped fiber amplifier (EDFA) was employed before Cir1 to compensate for the insertion loss of the IQM, such that the sensing fiber is still single span. Since the ratio of forward light intensity to RBS intensity can be approximated by a constant along the sensing fiber, using an EDFA to increase the light intensity does not alter the ratio between the RBS and forward light intensities. On the other hand, extracting the intermediate frequency (IF) signal via a digital bandpass filter can also effectively suppress the ASE (amplified spontaneous emission) noise from the EDFA, thereby avoiding the need for an additional optical bandpass filter. Due to the unidirectional isolation characteristic of Cir2 at the termination end, the RBS generated within the far-end segment cannot re-enter the sensing fiber. Consequently, a spectral separation is realized in the interference intensity spectrum between I_{FW} and I_{RBS}. By calculating the power ratio between I_{FW} and I_{RBS} within specific frequency bands, the signal-to-noise ratio (SNR_{rbs}) of I_{FW} relative to I_{RBS} can be determined, and expressed by the following equation:

$$SNR_{rbs} = 10\log(\frac{P_{FW}}{P_{RBS}}) \tag{25}$$

$$P_{FW} = \int_{\tau_L\gamma}^{+\infty} PSD_{I_s}(f)df \tag{26}$$

$$P_{RBS} = \int_{0}^{\tau_L\gamma} PSD_{I_s}(f)df \tag{27}$$

where P_{FW} and P_{RBS} are the frequency band power of I_{FW} and I_{RBS}, respectively. The calculated PSD results for I_s under different sensing distances are plotted in Fig. 4(a-e).

Figure 4(f) reveals that as the sensing distance increases, the bandwidth of I_{RBS} gradually grows from 9.84 MHz (20 km) to 58.94 MHz (120 km), resulting in a proportional increase in its occupancy across the entire frequency domain. In the RBS region of Fig. 4(c-e), reflection peaks resulting from flange connections are visible, which occur at the junctions between multiple fiber sections as well as at the distal end of the sensing fiber. Within the 20-70 km sensing range, reflection peaks originating from fiber connector interfaces are distinctly visible at the high-frequency end of the I_{RBS} spectrum, enabling straightforward identification of frequency bands containing this phenomenon. Although reflection peaks become less discernible beyond 100 km, the maximum beat frequency can still be calculated using $f_{rbs} = \gamma\tau_l, \tau_l \in [0, \tau_L]$ to determine the relevant spectral boundaries. Due to optical fiber propagation loss, the optical power of I_{FW} progressively decreases, resulting in a corresponding reduction in SNR_{rbs}. At 70 km, P_{RBS} exceeds that of P_{FW} by over 32.47 dB. When the sensing fiber length extends to

Optics EXPRESS

120 km, P_{FW} attenuates to -93.61 dBV^2, with the SNR_{rbs} reaching -72.07 dB. By tailoring the bandpass filters to selectively extract signals I_1 and I_2 while filtering out I_{RBS}, the SNR_{rbs} can be significantly enhanced, thus improving the SNR of $\phi_1(t)$ and $\phi_2(t)$.

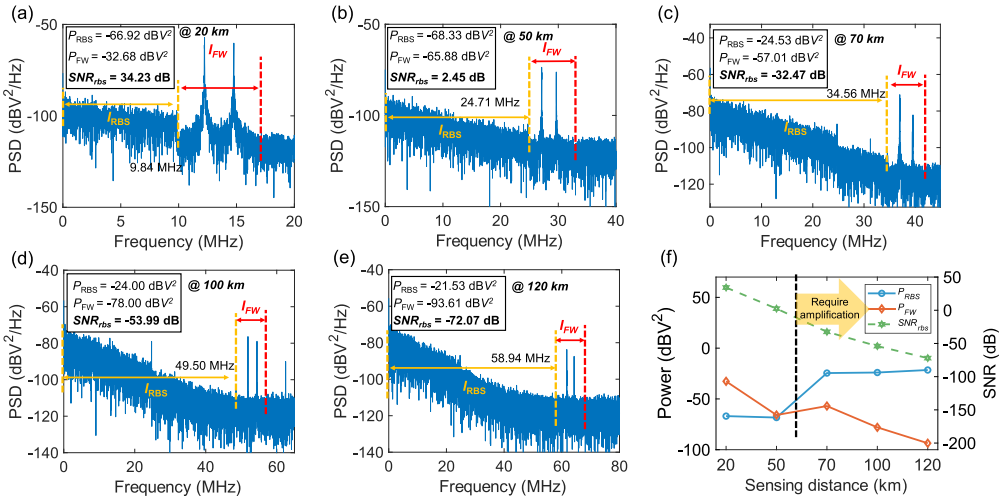

Fig. 4. Power Spectral Density (PSD) of I_s under different sensing distances: (a) 20 km; (b) 50 km; (c) 70 km; (d) 100 km; (e) 120 km; (f) P_{FW}, P_{RBS} and SNR_{rbs} as a function of sensing distance. Starting from 70 km, EDFA amplification is added prior to the sensing fiber to compensate for the optical loss of the IQM.

To investigate the system noise and its frequency response, the phase noise of the system is analyzed by calculating its PSD. First, a segment of I_s without external disturbance is acquired. Direct Hilbert transform demodulation is performed, and the PSD of the demodulated phase is calculated, then the in-band phase noise *Noise_I*$_s$ is evaluated by summing all phase components within the detection bandwidth (0-125 MHz). For comparison with optimal-bandwidth conditions, bandpass filters are used to extract the signals I_1 and I_2 separately. Each signal is demodulated via Hilbert transform, and the PSD of their respective demodulated phases ϕ_1 and ϕ_2 are calculated, and their individual in-band phase noise *Noise_I*$_1$ and *Noise_I*$_2$ are evaluated. The PSD results for phase noise of I_s, I_1 and I_2 are shown in Fig. 5(a). It can be observed that the PSD of the phase noise for I_s is significantly higher than that of I_1 and I_2. The corresponding in-band phase noise values are: 1371.78 rad, 81.03 rad, and 17.46 rad respectively. Due to the longer path length of TDF2 compared to that of TDF1, the phase noise of I_2 is greater than that of I_1. When a PZT with the voltage-strain coefficient of 0.092 με/V was placed at the end of the sensing fiber and driven with a 2 kHz, 5 Vpp sinusoidal signal, the PSD results of the demodulated phase are shown in Fig. 5(b). For the phase signal of I_s, the 2 kHz component is indistinguishable in the frequency domain due to dominance from RBS noise. In contrast, distinct peaks at 2 kHz are clearly visible in the frequency domain of both I_1 and I_2. Their respective demodulated phase SNRs: *SNR_*Φ_1 and *SNR_*Φ_2 can be expressed by: $10\log(P(\phi_1)/P(Noise\_I_1)$ and $10\log(P(\phi_2)/P(Noise\_I_2)$ respectively. In this experiment, *SNR_*Φ_1 and *SNR_*Φ_2 were measured to 33.11 dB and 32.67 dB, respectively. These results illustrate that the system phase noise is predominantly governed by RBS in I_s, exhibiting significant in-band phase noise. However, by isolating signals I_1 and I_2 using bandpass filters, the phase noise can be dramatically reduced. Hence, the CFS-FTDVS system enables long-distance vibration sensing with high signal fidelity.

Optics EXPRESS

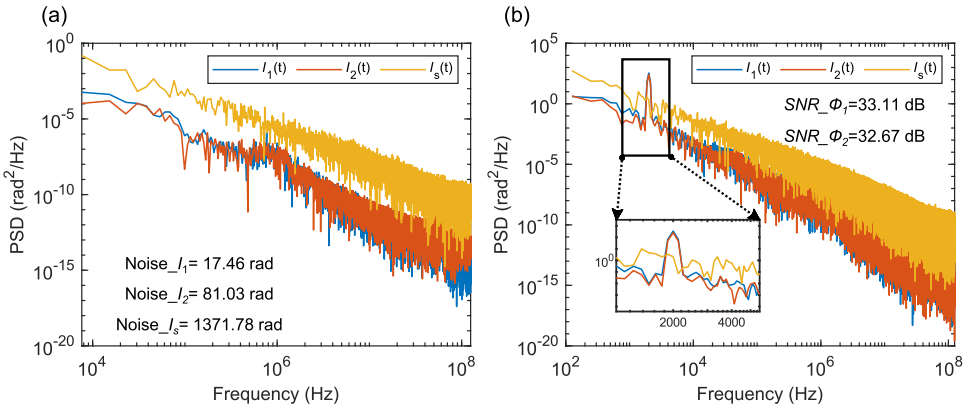

Fig. 5. Phase noise evaluation for 120 km sensing distance: (a) PSD of system phase noise. *Noise_I*$_s$: in-band phase noise of I_s, *Noise_I*$_1$: in-band phase noise of I_1, *Noise_I*$_2$: in-band phase noise of I_2; (b) PSD of demodulated phase with 2 kHz sinusoidal vibration *SNR_*Φ_1: SNR of ϕ_1, *SNR_*Φ_2: SNR of ϕ_1, *P*: Power.

3.2. Sensitivity and limit of detection analysis

Figure 6 presents the relationship between sinusoidal strain and reconstructed phases D_1 and D_2. With the PZT positioned at the sensing fiber end (121.32 km), applied voltages of 4-12 V induced corresponding strains between 0.37-1.10 με. Linear fitting of mean values from 10 repeated trials (Fig. 6(a)) revealed the following strain sensitivities for D_1: 66.12 rad/με @ 750 Hz, 99.12 rad/με @ 1000 Hz, and 146.52 rad/με @ 1500 Hz. For D_2 (Fig. 6(b)), the sensitivities are 74.19 rad/με @ 750 Hz, 93.66 rad/με @ 1000 Hz, and 134.41 rad/με @ 1500 Hz. As D_1 and D_2 are differential signals derived from the two time-delayed phase signals, their amplitudes depend on the vibration frequency. Consequently, the system sensitivity also varies with frequency and exhibits a linear relationship with it. The measured sensitivity ratios at these vibration frequencies are approximately 1:1.5:2.2 and 1:1.3:1.8 for the two parameters, respectively.

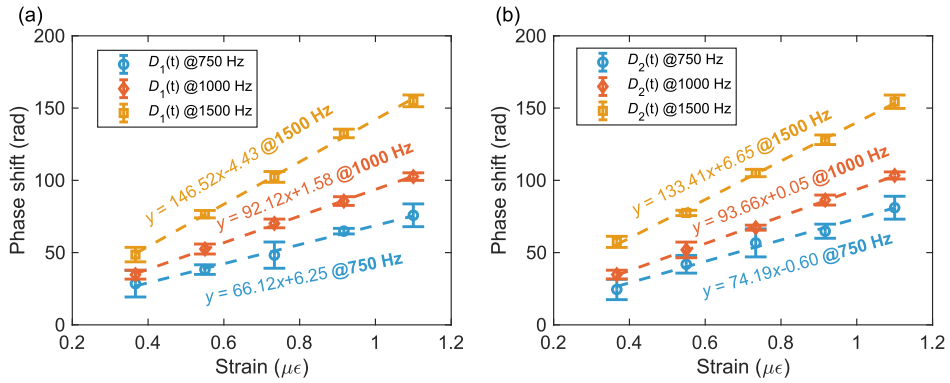

Fig. 6. Strain response and sensitivity at 121.323 km: (a) Phase shift of D_1 with varying strain at different frequencies; (b) Phase shift of D_2 with varying strain at different frequencies.

The limit of detection (LoD) of the sensing system can be calculated by the following formula:

$$LoD = \frac{mean(D_n)}{sensitivity \times \sqrt{B}} \tag{28}$$

Optics EXPRESS

where D_n represents the integrated amplitude measured over the effective bandwidth under vibration-free conditions. The values obtained from D_1 is 32.20 rad and D_2 is 32.40 rad, while B denotes the bandwidth of the BPD (200 MHz). The discrepancy between the D_n values of the two paths stems from the difference in their optical lengths and thus different cumulative phase noise: the path experienced by E_2 is approximately 10 km longer than that of E_1.

The LoD deduction under different frequencies are shown in Table 1, which indicates that the sensitivity progressively increases while the LoD decreases with rising vibration frequency. At 1500 Hz, sensitivity is 146.52 rad/με and the LoD is 15.54 pε/Hz$^{1/2}$. However, the frequency response range is constrained by the lengths of the two delay fibers and the frequency sweep rate. Higher vibration frequencies cause spectral aliasing between I_1 and I_2, compromising their separation. The max frequency response is $f_{max} < \gamma\Delta t/2$. Increasing either the sweep rate or delay fiber length elevates the beat frequency beyond practical sampling capabilities. Therefore, an appropriate choice of delay fiber lengths and sweep parameters is critical for optimal performance.

Table 1. The sensing performance at a position of 120 km with different vibration frequencies

Frequency (Hz)	D_1(t)			D_2(t)		
	Sensitivity (rad/με)	D_n (rad)	LoD (pε/Hz$^{1/2}$)	Sensitivity (rad/με)	D_n (rad)	LoD (pε/Hz$^{1/2}$)
750	66.12	32.20	34.44	74.19	32.40	30.69
1000	99.12		22.97	93.66		24.31
1500	146.52		15.54	134.41		17.05

Eq. (17–18) indicate that the sensing optical field E_s experiences the same external perturbation φ twice with position-dependent time delays upon returning to Rx. Consequently, the amplitude response of ϕ_1 and ϕ_2 exhibit frequency- and position-dependent variations. With the PZT strain value set to 0.7360 με, vibration frequency of 1000 Hz, and position at 120 km as the baseline, the phase shift of ϕ_1, ϕ_2, D_1 and D_2 are now 425.97 rad, 408.66 rad, 70.18 rad and 67.25 rad respectively. Figure 7(a) and (c) present simulated phase amplitudes as functions of frequency and vibration position. In Fig. 7(a) (vibration at 120 km, 100-2000Hz sinusoidal signals), the phase shift for both ϕ_1 and ϕ_2 components decrease nonlinearly with increasing frequency. Figure 7(c) demonstrates the position-dependent amplitude variation at 1000 Hz, where the relationship exhibits oscillatory behavior. As described in Eq. (17) and (18), $\phi_1(t)$ and $\phi_2(t)$ represent the superposition of two phase components. The $\phi_2(t)$ component approaches zero near 80 km due to destructive interference (time delay t_2 equals to half of the vibration signal period). Conversely, the reconstructed phases D_1 and D_2 exhibit a frequency-dependent linear increase with very similar slopes of 6.93 and 6.64, respectively (Fig. 7(b)). The responses of D_1 remain spatially consistent along the sensing fiber, showing negligible variation (maximum difference: 0.005 rad) as shown in Fig. 7(d). These results facilitate calibration of measured data to account for possible variations depending on the perceived vibration frequency and position.

3.3. Vibration positioning analysis

To validate the vibration demodulation and positioning ability of the sensing system, a sensing fiber with a length of 121,353 m was employed. A piezoelectric transducer (PZT) with 60 m of coiled fiber (calibrated) was positioned at the distal end of the sensing fiber to create vibrations along the sensing fiber. Sinusoidal signals at 2 kHz and sinc signals at 300 Hz were respectively applied to the PZT as driving signals. With the sweep period set to 10 ms, the corresponding waveform acquisition duration is 10 ms. Setting the vibration frequency above 100 Hz allows the acquisition of a greater number of waveform cycles, thereby improving the accuracy of

Optics EXPRESS

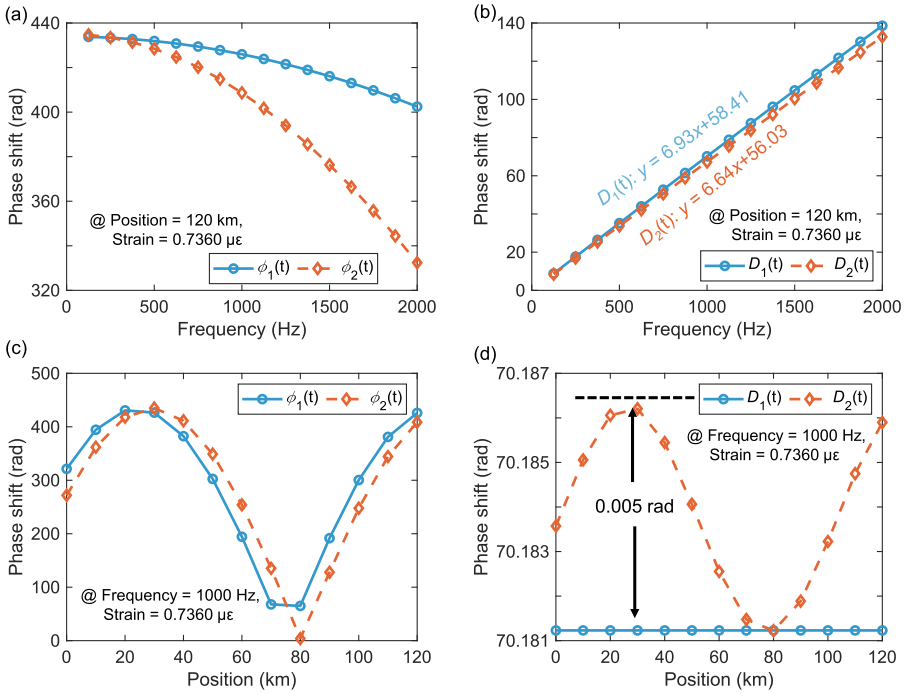

Fig. 7. Simulations of phase shift as functions of frequency and vibration position (a) Phase shift of ϕ_1 and ϕ_2 as a function of frequency; (b) Phase shift of D_1 and D_2 as a function of frequency; (c) Phase shift of ϕ_1 and ϕ_2 as a function of vibration position; (d) Phase shift of D_1 and D_2 as function of vibration position.

time-delay estimation. During system configuration, the sweep period can be adjusted flexibly to accommodate a wider frequency response range. However, an upper limit to the sweep period would be considered to avoid significantly reducing the measurement rate (refresh rate). During system configuration, the sweep period can be adjusted flexibly to accommodate a wider frequency response range. To extract I_1 and I_2 while mitigating the impact of I_{RBS}, two FIR equiripple bandpass filters were configured to eliminate I_s. The passbands of bandpass filter 1 and 2 are designed at 60.7–62.7 MHz and 63.4–65.4 MHz, respectively. Figure 8(a) and (b) present the STFT results of I_s under the two distinct vibration conditions. As observed in the results, the influence of external vibrations induces corresponding time-frequency variations at center frequencies of 61.75 MHz and 64.28 MHz, signifying that the vibrations generate phase shifts in both I_1 and I_2. Phase demodulation was performed on I_1 and I_2, with the results presented in Fig. 8(c) and (d). Due to effective mitigation of noise interference from I_{RBS}, the demodulated phase signals exhibit relatively high SNR. Furthermore, the reconstructed phases D_1 and D_2 exhibit high correlation with quantifiable time delay. The cross-correlation analysis deduced time delays of 0.101 ms and 0.104 ms, respectively. Substituting these values into Eq. (24) leads to calculated vibration positions of 121,014 m and 120,702 m, corresponding to positioning errors of 309 m and 621 m from the actual vibration position. It should be stressed that such discrepancies can be reduced through mean-position or fiber length calibration.

To validate the positioning ability of the sensing system at different positions along the sensing fiber, the PZT was sequentially placed at the junctions of three fiber links (lengths: 50,564 m, 50,585 m and 20,144 m) to allow testing of vibrations at distinct locations. The actual vibration positions (midpoints of PZT-coiled fiber) were set at 30 m (A), 50,594 m (B), 101,179 m (C), and 121,323 m (D), as illustrated in Fig. 9(e). Then, 64 successive measurements per position were

Optics EXPRESS

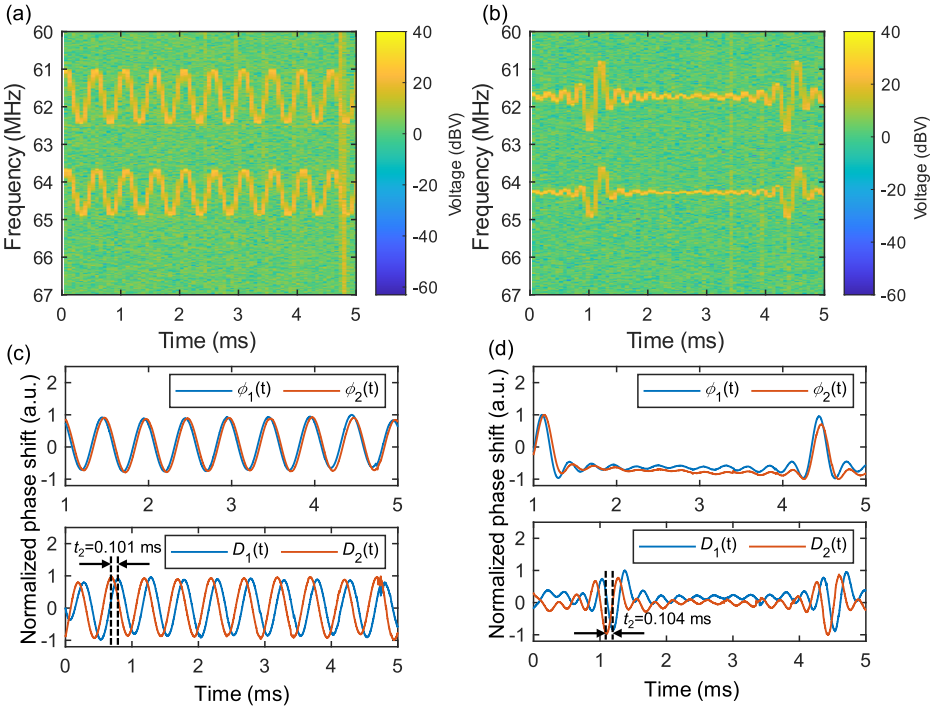

Fig. 8. Vibration signal analysis: STFT of I_s with (a) 2 kHz sinusoidal signal; and (b) 300 Hz sinc signal; Demodulated phase ϕ_1 and ϕ_2, reconstructed phase D_1 and D_2 of (c) 2 kHz sinusoidal signal; (d) 300 Hz sinc signal.

carried out using a 300 Hz periodic sinc drive signal, with reconstructed phases D_1 and D_2 shown in Fig. 9(a)–(d) and positioning results in Fig. 9(f). For position A, a cross-correlation-derived delay of t_2= 1.268 ms corresponds to a calculated position of −174 m (error: 204 m), with a mean position of −100 m (error: 130 m, STD: 85.09 m). For position B, t_2= 0.795 ms leads to 50,114 m (error: 480 m), with a mean value of 50,087 m (error: 507 m, STD: 158.29 m). For position C, t_2= 0.298 ms denotes 100,851 m (error: 328 m), with a mean value of 100,914 m (error: 265 m, STD: 133.29 m). Lastly, for position D, t_2= 0.101 ms represents 121,014 m (error: 309 m), with a mean value of 120,954 m (error: 369 m, STD: 133.37 m). The experiment results indicate that despite substantial positioning errors— maximum error of 507 m at Position B (STD: 158.29 m)—positioning remains feasible and consistent at all tested positions along 121 km of sensing fiber, unlike previous reports using double-ended configurations [11]. The variation in positioning accuracy at different positions is attributed to the influence from time- and space-dependent environmental noise during measurements. Additionally, changes in the state of polarization within the sensing fiber also affect the positioning accuracy. The discrepancy between the measured position and the actual position arises from deviations in the fiber effective index used in calculations versus its true value. In practical applications, this can be mitigated by back-calculating compensation values from the mean positioning values to recalibrate the total length of the sensing fiber.

To illustrate that the sensing system can work effectively in a complex environment with multiple concurrent vibration events, multi-point vibration positioning was demonstrated using the phase-spectrum time delay method [25]. During the experiment, 70.783 km of sensing fiber was connected with 2 PZTs inserted at the mid-point (50.571 km) and the far end (70.753 km) of the sensing fiber. Sinusoidal drive signals at 1.5 kHz and 2.5 kHz were applied to the PZTs. The

Optics EXPRESS

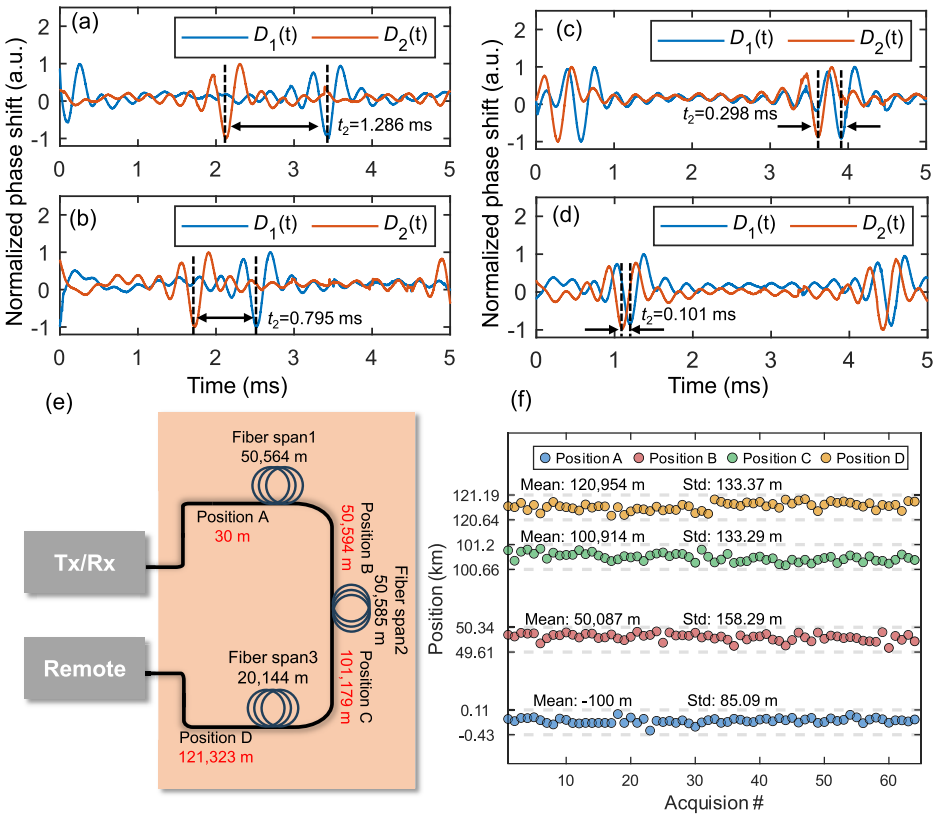

Fig. 9. Vibration measurements at different positions: Reconstructed phase at (a) position A (30 m); (b) Position B (50,594 m); (c) Position C (101,179 m); (d) Position D (121,323 m); (e) Fiber links forming the sensing fiber; (f) Positioning reproducibility of 64 successive measurements. STD: standard deviation.

reconstructed phase signals are shown in Fig. 10(a). It can be observed that the signals at $D_1(t)$ and $D_2(t)$ correspond to the superposition of the two sinusoidal signals and exhibit a high degree of correlation. The amplitude spectrum of the reconstructed phase signals, obtained via the Fast Fourier Transform (FFT), are plotted in Fig. 10(b). Two distinct peaks are clearly visible at 1.5 kHz and 2.5 kHz, consistent with the actual vibration frequencies. The time-delay spectrum, derived from the phase spectrum of the Fourier transform of the cross-correlation results, is shown in Fig. 10(c). The time delays corresponding to 1.5 kHz and 2.5 kHz were measured as 0.296 ms and 0.099 ms, respectively. Substituting these values into Eq. (24) yieldes calculated vibration positions of 50.601 km and 70.665 km, respectively. The resulting positioning errors are only 29 m and 88 m compared to the actual positions. To further evaluate the stability of the sensing system for multi-point vibration positioning, 32 repeated positioning measurements were conducted. The experiment results are summarized in Fig. 10(d). Over the 32 trials, the mean position near the 50 km mark is 50.606 km, with an error of 35 m relative to the actual position and a STD of 56.03 m. Near the 70 km mark, the mean position is 70.676 km, with an error of 107 m and an STD of 70.73 m. This demonstrates that the positioning of multiple vibrations is feasible at the basic level.

Optics EXPRESS

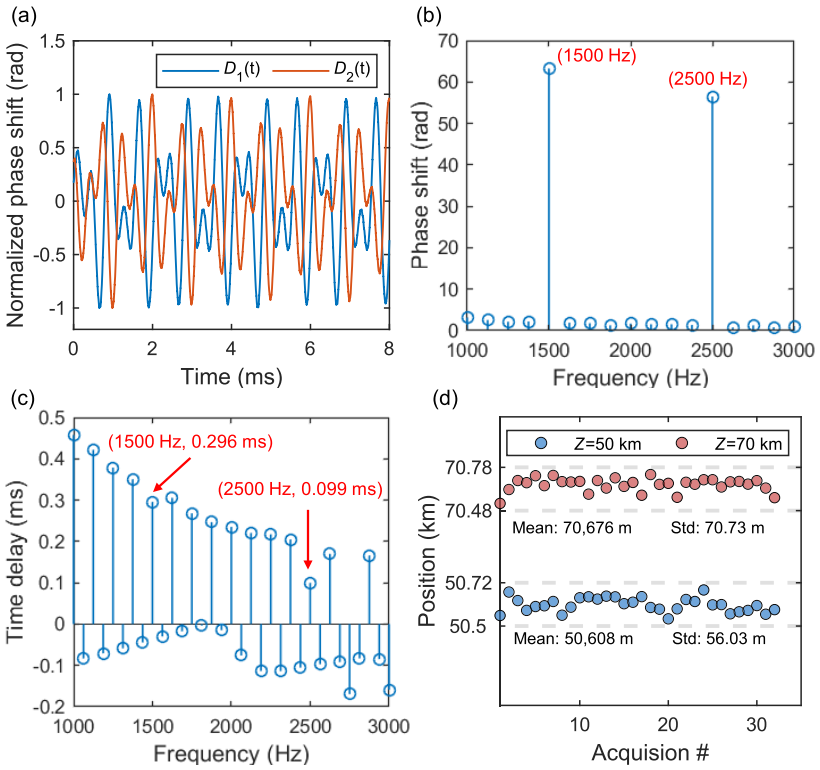

Fig. 10. Multi-point vibration measurements: (a) Phase signal of two vibration points; (b) Phase amplitude spectrum from FFT; (c) Phase-spectrum time delay analysis; (d) Positioning reproducibility of 32 successive measurements.

4. Conclusion

This work advances single-ended, ultra-long-distance distributed sensing technology through the demonstration of a forward-transmission distributed fiber-optic vibration (FTDVS) system based on chirped frequency-swept modulation and passive-terminal design. The system employs an I/Q modulator to generate single-sideband modulated chirped frequency-swept probe signals. Through two terminal-end delay fibers of different lengths, forward-propagating light paths can be precisely extracted via frequency-domain methods, while Rayleigh backscatter (RBS) noise is spectrally isolated. This practical implementation can use standard telecom single-mode fiber with single-channel analog-to-digital data acquisition. Overall, the proposed sensing system significantly reduces complexity and cost compared to prior art. The experimental validation demonstrated a 120 km sensing distance without inline amplification, and an 85 m position accuracy (STD), despite extremely weak forward-transmitted signal conditions (72 dB below RBS). The system sensitivity is 146.52 rad/με and the LoD is 15.54 pε/Hz$^{1/2}$ at 1500 Hz. The frequency response range is 100 Hz – 1 MHz under a sweep frequency cycle of 10 ms. Furthermore, multi-point vibration positioning was verified over 70 km with 56 m position accuracy, by using a phase-spectrum-based signal processing method.

Optics EXPRESS

Appendix A

A.1 Multi-path RBS power analysis

Owing to the unidirectional isolation property of Cir2 in Fig. 1(a), the RBS of the optical field E_s can be divided into five paths. The most significant contribution to the forward optical field E_1 and E_2 comes from E_{rbs} described in Section 2.1. When the sensing fiber length exceeds 65 km, the optical power of E_{rbs} surpasses that of the E_1 and E_2 due to the integration of RBS at the Rx. The remaining four path of RBS optical fields E_{rbs2}, E_{rbs3}, E_{rbs4} and E_{rbs5} are as follows:

$Path_{RBS2}$: Sensing fiber→TDF1→Sensing fiber→TDF1→Cir2→Sensing fiber→Cir1→OC4
$Path_{RBS3}$: Sensing fiber→TDF2→Sensing fiber→TDF2→Cir2→Sensing fiber→Cir1→OC4
$Path_{RBS4}$: Sensing fiber→TDF1→Sensing fiber→TDF2→Cir2→Sensing fiber→Cir1→OC4
$Path_{RBS5}$: Sensing fiber→TDF2→Sensing fiber→TDF1→Cir2→Sensing fiber→Cir1→OC4

Given an initial optical power of P_0, we can establish a model for the optical power received by Rx from each optical field as a function of fiber length L, enabling the analysis of how the RBS optical field from different paths influence the forward optical fields. According to the optical power attenuation formula, the optical powers P_1 and P_2 of E_1 and E_2 returning to Rx through the sensing fiber are given by:

$$P_1(L) = P_0 \exp(-\alpha(2L + L_1)) \tag{29}$$

$$P_2(L) = P_0 \exp(-\alpha(2L + L_2)) \tag{30}$$

The optical power P_{RBS} received at Rx from E_{rbs} (dominant component in the RBS) can be expressed as:

$$P_{RBS}(L) = P_0 \alpha_s \sum_{z=0}^{L} \exp(-2\alpha z) \tag{31}$$

where α_s is the Rayleigh backscattering coefficient of the fiber, α is the attenuation coefficient, and z represents the nominal scattering point along the sensing fiber where the Rayleigh backscattering is generated. Taking E_{rbs2} as an example, the optical power P_{RBS2} received at Rx can be expressed as:

$$\begin{aligned} P_{RBS2}(L) = P_0 \sum_{z=0}^{L} &\exp(-\alpha L) \times \exp(-\alpha L_1) \times \exp(-\alpha(L - z)) \\ &\times \alpha_s \exp(-\alpha(L - z)) \times \exp(-\alpha L_1) \times \exp(-\alpha L) \end{aligned} \tag{32}$$

The first term corresponds to the path traveled by the forward light to the nominal scattering point at position z, while the second term describes the path of the Rayleigh backscattering from point z through Cir2 back into the sensing fiber and finally to Rx. Following the same logic, P_{RBS3}, P_{RBS4} and P_{RBS5} can be expressed respectively as:

$$\begin{aligned} P_{RBS3}(L) &= P_0 \sum_{l=0}^{L} \exp(-\alpha L) \times \exp(-\alpha L_2) \times \exp(-\alpha(L - z)) \\ &\times \alpha_s \exp(-\alpha(L - z)) \times \exp(-\alpha L_2) \times \exp(-\alpha L) \\ &= P_0 \sum_{l=0}^{L} \exp(-4\alpha L - 2\alpha L_2 + 2\alpha z) \end{aligned} \tag{33}$$

Optics EXPRESS

$$
\begin{aligned}
P_{RBS4}(L) &= P_0 \sum_{l=0}^{L} \exp(-\alpha L) \times \exp(-\alpha L_1) \times \exp(-\alpha(L-z)) \\
&\quad \times \alpha_s \exp(-\alpha(L-z)) \times \exp(-\alpha L_2) \times \exp(-\alpha L) \\
&= P_0 \sum_{l=0}^{L} \exp(-4\alpha L - \alpha(L_1 + L_2) + 2\alpha z)
\end{aligned} \tag{34}
$$

$$
\begin{aligned}
P_{RBS5}(L) &= P_0 \sum_{l=0}^{L} \exp(-\alpha L) \times \exp(-\alpha L_1) \times \exp(-\alpha(L-z)) \\
&\quad \times \alpha_s \exp(-\alpha(L-z)) \times \exp(-\alpha L_2) \times \exp(-\alpha L) \\
&= P_0 \sum_{l=0}^{L} \exp(-4\alpha L - \alpha(L_1 + L_2) + 2\alpha z)
\end{aligned} \tag{35}
$$

The simulation results of P_1, P_2, P_{RBS}, P_{RBS2}, P_{RBS3}, P_{RBS4} and P_{RBS5} as a function of distance are shown in Fig. 11. It can be observed that P_{RBS} surpasses P_1 and P_2 at sensing distances beyond 65 km. However, this dominant noise component is removable by employing a bandpass filter to isolate the forward interference signals I_1 and I_2. In contrast, the components from P_{RBS2} to P_{RBS5} are consistently attenuated by more than 31 dB relative to P_1 and P_2 for all distances, rendering them as negligible background noise.

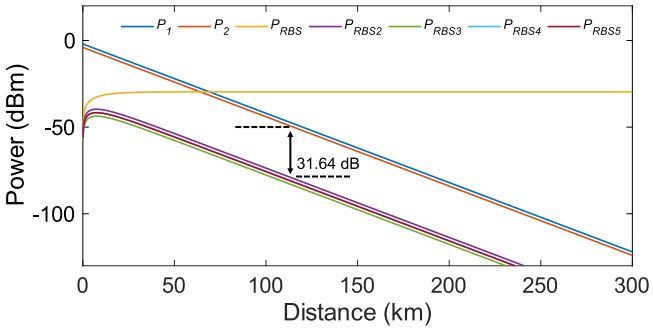

Fig. 11. Simulation results of P_1, P_2, P_{RBS}, P_{RBS2}, P_{RBS3}, P_{RBS4} and P_{RBS5} as a function of distance.

Funding. National Natural Science Foundation of China (W2532046, 62275172, U22A2088); Shenzhen Science and Technology Program (JCYJ20241202124408012, JCYJ20220818095800001); Shenzhen Science and Technology Program (Shenzhen Key Laboratory of Ultrafast Laser Micro/Nano Manufacturing) (ZDSYS20220606100405013); Scientific Instrument Developing Program of Shenzhen University (2023YQ027); Research Team Cultivation Program of Shenzhen University (2023DFT001)

Disclosures. The authors declare no conflicts of interest.

Data availability. Data underlying the results presented in this paper are not publicly available at this time but may be obtained from the authors upon reasonable request.

References

1. K. Liu, X. Jin, J. Jiang, *et al.*, "Interferometer-based distributed optical fiber sensors in long-distance vibration detection: A review," IEEE Sens. J. **22**(22), 21428–21444 (2022).
2. Y. Yan, F. N. Khan, B. Zhou, *et al.*, "Forward transmission based ultra-long distributed vibration sensing with wide frequency response," J. Lightwave Technol. **39**(7), 2241–2249 (2021).
3. B. Yang, J. Tang, C. Cheng, *et al.*, "Integrated communication and enhanced forward phase-based sensing based on frequency-domain pilot tones in DSCM systems using 100 kHz ECLs," J. Lightwave Technol. **43**(6), 2664–2671 (2025).

Optics EXPRESS

4. Y. Yan, L. Lu, X. Wu, *et al.*, "Simultaneous communications and vibration sensing over a single 100-km deployed fiber link by fiber interferometry," in *Optical Fiber Communications Conference and Exhibition*, (SPIE, 2023), 1–3.
5. E. Ip, Y.-K. Huang, G. Wellbrock, *et al.*, "Vibration detection and localization using modified digital coherent telecom transponders," J. Lightwave Technol. **40**(5), 1472–1482 (2022).
6. J. Tang, X. Li, C. Cheng, *et al.*, "Forward-transmission based distributed fiber sensing compatible with C + L unidirectional communication systems," in *Optical Fiber Communications Conference and Exhibition*, (SPIE, 2024), 1–3.
7. G. Marra, C. Clivati, R. Luckett, *et al.*, "Ultrastable laser interferometry for earthquake detection with terrestrial and submarine cables," Science **361**(6401), 486–490 (2018).
8. Z. Zhan, M. Cantono, V. Kamalov, *et al.*, "Optical polarization–based seismic and water wave sensing on transoceanic cables," Science **371**(6532), 931–936 (2021).
9. G. Marra, D. M. Fairweather, V. Kamalov, *et al.*, "Optical interferometry–based array of seafloor environmental sensors using a transoceanic submarine cable," Science **376**(6595), 874–879 (2022).
10. G. Wang, Z. Pang, B. Zhang, *et al.*, "Time shifting deviation method enhanced laser interferometry: ultrahigh precision localizing of traffic vibration using an urban fiber link," Photonics Res. **10**(2), 433–443 (2022).
11. G. Wang, D. Song, Z. Pang, *et al.*, "Laser interferometry for high-speed railway health inspection using telecom fiber along the line," Nat. Commun. **16**(1), 4129 (2025).
12. Z. Sun, D. Sun, H. Yang, *et al.*, "Distributed optical fiber vibration sensors using light interference technology: fundamental principles and major advancements," IEEE Trans. Instrum. Meas. **74**, 1–27 (2025).
13. G. Y. Chen, K. Liu, X. Rao, *et al.*, "Long-range distributed vibration sensing using phase-sensitive forward optical transmission," Opt. Lett. **48**(18), 4825–4828 (2023).
14. G. Y. Chen, X. Rao, K. Liu, *et al.*, "Super-long-range distributed vibration sensor based on the polarimetric forward-transmission of light," Opt. Lett. **48**(21), 5767–5770 (2023).
15. X. Rao, Y. Wang, M. Chen, *et al.*, "150 km single-span distributed vibration sensor based on compensated self-interference forward transmission," J. Lightwave Technol. **42**(16), 5736–5742 (2024).
16. X. Fang, "Fiber-optic distributed sensing by a two-loop Sagnac interferometer," Opt. Lett. **21**(6), 444–446 (1996).
17. J. Ali, A. Almaiman, A. M. Ragheb, *et al.*, "Multievent localization for loop-based Sagnac sensing system using machine learning," Opt. Express **31**(15), 24005–24024 (2023).
18. J. P. Kurmer, S. A. Kingsley, J. S. Laudo, *et al.*, "Distributed fiber optic acoustic sensor for leak detection," in *Distributed and Multiplexed Fiber Optic Sensors*, (SPIE, 1992), 117–128.
19. Z. Ye, J. Wang, C. Wang, *et al.*, "A positioning algorithm realized multilateration for distributed fiber-optic sensor," Micro & Optical Tech Letters **58**(12), 2913–2917 (2016).
20. J. Huang, Y. Chen, Q. Xiao, *et al.*, "A novel Sagnac distributed optical fiber vibration sensor based on time delay estimation algorithm," in *Optics Frontiers Online 2020: Distributed Optical Fiber Sensing Technology and Applications*, (SPIE, 2021), 24–28.
21. K. Liu, P. Ma, J. Jiang, *et al.*, "An S-transform-based positioning method for asymmetric interferometer disturbance sensors," J. Lightwave Technol. **37**(13), 3201–3207 (2019).
22. W. Kong, X. Fan, F. Ito, *et al.*, "Localization enhancement of forward-transmission distributed vibration sensors using phase differentiation endpoint amplification," IEEE Sens. J. **24**(11), 17669–17676 (2024).
23. Y. Koshikiya, X. Fan, and F. Ito, "Long range and cm-level spatial resolution measurement using coherent optical frequency domain reflectometry With SSB-SC modulator and narrow linewidth fiber laser," J. Lightwave Technol. **26**(18), 3287–3294 (2008).
24. Z. Wang, L. Zhang, S. Wang, *et al.*, "Coherent Φ-OTDR based on I/Q demodulation and homodyne detection," Opt. Express **24**(2), 853–858 (2016).
25. X. Rao, S. Dai, M. Chen, *et al.*, "Multi-point vibration positioning method for long-distance forward transmission distributed vibration sensing," Opt. Express **32**(17), 30775–30786 (2024).

https://doi.org/10.1364/OE.573036 Received 06 Oct 2025; Revised 20 Nov 2025; Accepted 20 Nov 2025; Published 29 Dec 2025